

**MIXING IN A BASIC OXYGEN FURNACE (BOF) UNDER  
COMBINED BLOWING CONDITIONS: COLD-FLOW  
MEASUREMENTS AND DEVELOPMENT OF CFD MODEL**

**SAYANTAN BISWAS**



**DEPARTMENT OF CHEMICAL ENGINEERING  
INDIAN INSTITUTE OF TECHNOLOGY DELHI  
JULY 2025**

© Indian Institute of Technology Delhi (IITD), New Delhi, 2025

**Mixing in a Basic Oxygen Furnace (BOF) under Combined  
Blowing Conditions: Cold-flow Measurements and Development  
of CFD Model**

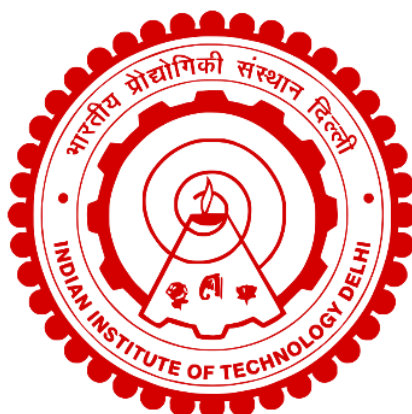
**Sayantana Biswas**

submitted

In the fulfilment of the requirements for degree of

**Doctor of Philosophy**

to the



Department of Chemical Engineering  
Indian Institute of Technology Delhi

July 2025

## Certificate

This is to certify that the thesis entitled “**Mixing in a Basic Oxygen Furnace (BOF) under Combined Blowing Conditions: Cold-Flow Measurements and Development of CFD Model**” being submitted by **Mr. Sayantan Biswas** to the **Indian Institute of Technology, Delhi** for the award of the degree of **Doctor of Philosophy** is a bonafide record of original research work carried out by him under my supervision in conformity with rules and regulations of the institute. The results contained in this thesis have not been submitted, in part or in full, to any other University or Institute for the award of any Degree or Diploma.

Date:

Dr Vivek V. Buwa

Professor

Department of Chemical Engineering,

Indian Institute of Technology Delhi,

New Delhi- 110016, India

## Acknowledgements

The past six years of my doctoral journey have been an exhilarating and transformative experience. This dissertation would not have been possible without the support, guidance, and encouragement of many individuals who, in various ways—academically, professionally, and personally—contributed to this endeavour. I am deeply grateful to each one of them.

First and foremost, I extend my heartfelt gratitude to my advisor, Prof. Vivek V. Buwa, for his unwavering support, patience, and insightful mentorship. His encouragement and belief in my abilities provided me with the confidence to push through challenges. I have been incredibly fortunate to have a mentor who not only guided me through the technical aspects of this research but also stood by me during moments of doubt, offering much-needed moral support. His constructive feedback and stimulating discussions have been instrumental in shaping this dissertation.

I am also sincerely thankful to my Ph.D. research committee members: Prof. Paresh Choksi, Prof. Vikram Singh, and Prof. Bhani Ray for their invaluable feedback and critical insights, which significantly contributed to refining my work. Their thoughtful suggestions and rigorous evaluations helped me navigate the research process more effectively.

I gratefully acknowledge the Tata Steel Research and Development Division, Jamshedpur, and the Foundation for Innovation and Technology Transfer (FIIT), IIT Delhi, for their generous financial support. Special thanks to Dr. Vikas Singh and Mrs. Soumya V. Nalluri from Tata Steel R&D Jamshedpur for their valuable discussions and technical inputs throughout this project. Additionally, I am thankful to the Industrial Research & Development Unit (IRD) for their assistance in facilitating conference travel, which greatly enriched my academic exposure.

I would also like to express my gratitude to my colleagues in the Multiphase Research Group Kuldeep, Ankita, Devesh, Sujata, Rohit, Sohela, Prantik, and Rajat for their discussions,

and thoughtful advice. A special mention to my senior colleagues, Dr. Aniket Ambekar, Dr. G.M. Karthik, Dr. Abhijit Thaker, Dr. Sirisha Parvathaneni, Mr. Sahil Bhujbal, and Mr. Vedit Tiwari, whose mentorship and shared experiences played a vital role in my academic and personal growth. I am also grateful to Mr. Anil Kumar for his invaluable assistance during the experimental phase of my research.

Beyond academia, my deepest gratitude goes to my family, whose unwavering love and sacrifices made this journey possible. Their encouragement, patience, and belief in me have been my greatest source of strength. A special note of thanks to my life partner, Srinanti Bagchi, for her constant support and understanding through every high and low. Her patience and encouragement have been instrumental in helping me persevere through the most demanding phases of this journey.

Finally, I thank all those named and unnamed who have contributed to this research and my personal growth in one way or another. This milestone is as much yours as it is mine.

Sayantana Biswas

## Abstract

The Basic Oxygen Furnace (BOF) is widely used to produce high-quality steel from pig iron as a part of the primary steel refining process. In this present work, we have simulated the dynamics of dispersed gas-liquid flow in a 6:1 scaled-down BOF vessel under cold-flow conditions using two two-fluid Euler-Euler method. The effect of interphase coupling forces (drag and non-drag forces) on the behaviour of multiple interacting bubble plumes are systematically investigated and a reasonable agreement is found with the corresponding measurements.

The experimentally- validated computational model is extended to the Eulerian multi-fluid approach to incorporate the slag layer. The implementation of three-phase interphase coupling forces in the Eulerian framework is analysed in detail. Cold flow measurements are performed to measure the ‘open-eye’ formation and the measurements are compared with the corresponding simulations for different mass flow rates and heights of the slag layer. The mixing time predicted by two-fluid Euler-Euler model (without slag layer) is compared with corresponding measurements and a good agreement is found for different mass flow rates. Further, the effect of the slag layer, its height, and physical properties (density and viscosity) on the liquid-phase hydrodynamics and mixing behaviour is numerically investigated. The spatial distribution of the slag layer and liquid-phase hydrodynamics is found to be significantly influenced by mass flow rate, height of the slag layer, and its density.

The bottom-blowing BOF model is integrated with a top-blowing lance consist of 4 converging-diverging nozzles to simulate dispersed gas-liquid flow under combined blowing conditions using two fluid Euler-Euler method. The cavity/ crater formation created by multiple impinging jets is compared with theoretical correlation. A reasonable agreement is found for wide different top blowing mass flow rate and lance height. Further, the effect of top-blowing

flow rates, and lance height on the liquid-phase hydrodynamics and mixing behaviour is investigated. We found liquid-phase mixing is found to be delayed as compared to bottom blowing in spite of the additional energy provided by the top blowing.

In a separate work, the rise of a bubble plume through two immiscible liquids is simulated using the Discrete Particle-Volume of Fluid (DPM-VOF) approach in a rectangular column. The relative contributions of different forces (inertial, gravitational, viscous, and interfacial tension) that govern the oil-water interface topology are investigated by varying the liquid properties systematically (density, viscosity, and interfacial tension) and operating conditions (thickness of oil layer, flow rate, and bubble size). We identified four different interface topologies and a regime map is proposed to characterize the interplay of governing forces using modified Froude ( $Fr^*$ ) and Capillary Number ( $Ca$ ).

The results presented in this thesis will help to understand the liquid-phase hydrodynamics and mixing behaviour generated by meandering multiple bubble plumes in presence of slag layer and in a scaled-down BOF vessel under bottom and combined blowing conditions. In addition, role of forces that govern liquid-liquid interface distribution when a bubble plume is rising through two immiscible liquid layer. The refining reactions kinetics and heat transfer can be integrated with the present computational model which will allow to simulate the commercial BOF vessel at actual conditions to improve its performance.

## सारांश:

बेसिक ऑक्सीजन फर्नेस (BOF) का व्यापक रूप से उपयोग कच्चा लोहे से उच्च गुणवत्ता वाला इस्पात बनाने के लिए प्राथमिक स्टील शोधन प्रक्रिया के एक भाग के रूप में किया जाता है। इस वर्तमान कार्य में, हमने ठंडे प्रवाह (cold-flow) की स्थिति में 6:1 स्केल-डाउन BOF पात्र में गैस-तरल प्रवाह की गतिशीलता का अनुकरण, दो-द्रव (Euler-Euler) विधि द्वारा किया है। इंटरफेज कपलिंग बलों (ड्रैग और गैर-ड्रैग बलों) का प्रभाव बहु-बबल प्लूम के व्यवहार पर व्यवस्थित रूप से अध्ययन किया गया और इसके परिणामों की तुलनात्मक मापनों से अच्छी संगति पाई गई।

प्रायोगिक रूप से मान्यीकृत इस गणनात्मक मॉडल को स्लैग परत को शामिल करने के लिए यूलरियन मल्टी-फ्लुइड दृष्टिकोण तक विस्तारित किया गया है। यूलरियन रूपरेखा में तीन-चरण इंटरफेज कपलिंग बलों के कार्यान्वयन का विस्तार से विश्लेषण किया गया है। "ओपन-आई" बनने की प्रक्रिया को मापने के लिए ठंडे प्रवाह के प्रयोग किए गए और अलग-अलग मास फ्लो दरों तथा स्लैग परत की ऊँचाई के लिए प्राप्त मापनों की संबंधित सिमुलेशन के साथ तुलना की गई। बिना स्लैग परत वाले दो-द्रव यूलर-यूलर मॉडल द्वारा पूर्वानुमानित मिक्सिंग समय की तुलना मापनों से की गई और विभिन्न फ्लो दरों के लिए अच्छी संगति देखी गई। इसके अतिरिक्त, स्लैग परत, उसकी ऊँचाई, और उसकी भौतिक गुणों (घनत्व और श्यानता) के प्रभाव का तरल-चरण गतिशीलता और मिश्रण व्यवहार पर संख्यात्मक रूप से अध्ययन किया गया। यह पाया गया कि स्लैग परत की स्थानिक संरचना और तरल की गतिशीलता को मास फ्लो दर, स्लैग परत की ऊँचाई, और घनत्व द्वारा महत्वपूर्ण रूप से प्रभावित किया जाता है।

बॉटम ब्लोइंग BOF मॉडल को चार संकुचन-विस्तारण नोजल वाली टॉप ब्लोइंग लांस के साथ जोड़ा गया है, ताकि सम्मिलित ब्लोइंग स्थितियों में दो-द्रव यूलर-यूलर विधि का उपयोग करते हुए गैस-तरल प्रवाह का अनुकरण किया जा सके। बहु-प्रभावी जेट्स द्वारा निर्मित गुफा/क्रेटर संरचना की तुलना सैद्धांतिक संबंधों से की गई और विभिन्न टॉप ब्लोइंग फ्लो दरों तथा लांस की ऊँचाई के लिए अच्छी संगति प्राप्त हुई।

आगे, टॉप ब्लोइंग फ्लो दरों और लांस ऊँचाई के तरल-चरण गतिशीलता और मिश्रण व्यवहार पर प्रभाव का अध्ययन किया गया। यह पाया गया कि टॉप ब्लोइंग के अतिरिक्त ऊर्जा के बावजूद, बॉटम ब्लोइंग की तुलना में तरल-चरण मिक्सिंग में विलंब होता है।

एक अन्य स्वतंत्र अध्ययन में, दो अमिश्रणीय तरल परतों के माध्यम से बबल प्लूम के उठने की प्रक्रिया का अनुकरण एक आयताकार स्तंभ में डिस्क्रीट पार्टिकल-वॉल्यूम ऑफ फ्लुइड (DPM-VOF) विधि से किया गया है। इस अध्ययन में तेल-पानी इंटरफेस की आकृति विज्ञान को नियंत्रित करने वाली विभिन्न बलों (जड़त्वीय, गुरुत्वीय, श्यान, और अंतरफलक तन्यता) के सापेक्ष योगदान का विश्लेषण किया गया है, जिसमें तरल गुणों (घनत्व, श्यानता और अंतरफलक तन्यता) और परिचालन स्थितियों (तेल परत की मोटाई, प्रवाह दर, और बबल का आकार) को व्यवस्थित रूप से परिवर्तित किया गया है। हमने चार विभिन्न इंटरफेस आकृतियों की पहचान की और एक रेजीम मैप प्रस्तावित किया है जो नियंत्रक बलों की अंतःक्रिया को संशोधित फ्रौड संख्या ( $Fr^*$ ) और कैपिलरी संख्या ( $Ca$ ) के माध्यम से दर्शाता है।

इस शोध में प्रस्तुत परिणाम तरल-चरण गतिशीलता और मिश्रण व्यवहार को समझने में सहायक होंगे, विशेषकर स्लैग परत की उपस्थिति में और स्केल-डाउन BOF पात्र में बहती बहु-बबल प्लूम की स्थिति में, बॉटम और सम्मिलित ब्लोइंग स्थितियों में। इसके अतिरिक्त, यह भी स्पष्ट होता है कि जब बबल प्लूम दो अमिश्रणीय तरल परतों के माध्यम से उठता है, तो तरल-तरल इंटरफेस वितरण को नियंत्रित करने वाले बलों की भूमिका क्या होती है। वर्तमान गणनात्मक मॉडल में परिशोधन अभिक्रियाओं की गति और ऊष्मा स्थानांतरण को भी जोड़ा जा सकता है, जिससे वास्तविक परिस्थितियों में वाणिज्यिक BOF पात्र का अनुकरण कर उसकी कार्यक्षमता को बेहतर बनाया जा सकेगा।

# Table of Contents

Certificate .....	i
Acknowledgements .....	ii
Abstract.....	iv
List of figures.....	xii
List of Table .....	xxii
Nomenclature .....	xxiii
<b>Chapter 1: Introduction .....</b>	<b>25</b>
1.1 Overview of steel making process .....	26
1.2 Motivation of the present thesis .....	32
1.3 Specific objectives.....	32
1.4 Organization of thesis .....	35
<b>Chapter 2: Eulerian multifluid Simulations of Gas-Liquid Flow in a Cold Flow Model of Basic Oxygen Furnace .....</b>	<b>38</b>
2.1 Introduction .....	39
2.2 Methodology .....	43
2.2.1 Experimental set up and image processing .....	44
2.2.2 Eulerian multifluid computational model .....	46
2.2.3 Numerical setup and boundary conditions.....	50
2.3 Simulation of unsteady gas-liquid flow using two-fluid model and experimental verification .....	51
2.3.1 Effect of momentum intercoupling forces on bubble plume distribution...54	
2.3.2 Effect of mass flow rate on the bubble plume behaviour and experimental verification.....	59
2.4 Simulation of dispersed gas-liquid flow in presence of slag layer and experimental verification.....	62
2.4.1 Development of Eulerian multifluid computational model.....	63
2.4.2 Effect of slag layer thickness on the slag layer distribution and comparison with measurements .....	66

2.4.3	Effect of mass flow rate on the slag layer distribution and comparison with experimental measurements .....	72
2.5	Summary and conclusions .....	77
<b>Chapter 3: Mixing Investigation in BOF using Eulerian Multifluid Approach: Effect of Top Liquid Layer .....</b>		
<b>80</b>		
3.1	Introduction .....	81
3.2	Methodology .....	85
3.2.1	Computational model .....	86
3.2.2	Numerical set-up and boundary conditions .....	88
3.3	Effect of slag layer thickness on the liquid-phase hydrodynamics .....	89
3.3.1	Effect of slag layer on liquid-phase turbulence .....	90
3.4	Effect of physical properties of slag layer on the liquid-phase hydrodynamics behaviour.....	93
3.4.1	Effect of physical properties of slag layer on the liquid-phase turbulence.....	97
3.5	Effect of slag layer on the liquid-phase mixing.....	98
3.5.1	Liquid-phase mixing without slag layer and comparison with measurements.....	98
3.5.2	Effect of slag layer thickness on liquid-phase mixing.....	100
3.5.3	Effect of physical properties of slag layer on liquid-phase mixing.....	109
3.6	Summary and conclusions .....	112
<b>Chapter 4: Eulerian Simulations of Liquid Phase Mixing in a Combined Blowing BOF: Effect of Top Blowing.....</b>		
<b>114</b>		
4.1	Introduction .....	115
4.2	Methodology .....	118
4.2.1	Computational model .....	119
4.2.2	Numerical setup and boundary conditions.....	124
4.3	Simulation of dispersed gas-liquid flow under combined blowing conditions	124
4.3.1	Numerical model validation .....	127

4.3.2	Effect of top blowing and its mass flow rate on the liquid-phase hydrodynamics.....	128
4.3.3	Effect of top blowing and its mass flow rate on the liquid-phase turbulence	135
4.3.4	Effect of top blowing lance height on the liquid-phase hydrodynamics ...	137
4.4	Effect of top blowing on liquid-phase mixing.....	141
4.4.1	Effect of top blowing mass flow rate of liquid-phase mixing.....	141
4.4.2	Effect of top blowing lance height on liquid-phase mixing .....	148
4.5	Summary and conclusions .....	151
<b>Chapter 5: Discrete Particle - Volume of Fluid Simulation of Bubble Plume Rising through Two Immiscible Liquid .....</b>		<b>153</b>
5.1	Introduction .....	154
5.2	Methodology .....	157
5.2.1	Experimental set up and measurements of top liquid-layer distribution .	157
5.2.2	Computational model .....	159
5.2.3	Geometry, boundary conditions and numerics .....	163
5.3	Preliminary simulations and verification with measurements.....	165
5.4	Effect of oil thickness and oil-phase density on the oil-water interface topology	171
5.5	Effect of oil viscosity and interfacial tension on bubble rise behaviour and oil-water interface topology .....	176
5.6	Effect of gas mass flow rate and bubble size on the oil-water interface topology	181
5.7	Effect of water viscosity on oil-water interface topology .....	185
5.8	Regime map .....	186
5.9	Summary and conclusions .....	188
<b>Chapter 6: Summary, Conclusions and Suggestions for Future Work.....</b>		<b>191</b>
6.1	Summary and conclusions.....	192
6.2	Overall contribution of the thesis .....	197

<b>6.3</b>	<b>Suggestions for future work .....</b>	<b>198</b>
	<b>References .....</b>	<b>199</b>
	<b>List of publications.....</b>	<b>207</b>
	<b>Bio-data.....</b>	<b>209</b>

## List of figures

Figure 1.1: Annual steel production in the world and in India. ....	26
Figure 1.2: Schematic of overview of steelmaking and refining process. ....	28
Figure 1.3: Schematic of different stages involved in BOF steel making process. ....	30
Figure 1.4: Schematic of different modes of gas blowing in BOF steel making process (a) top blowing, (b) bottom blowing and (c) combine blowing. ....	31
Figure 2.1: Schematic of (a) actual vessel and (b) 6:1 scaled-down model of BOF (all dimensions are in m). ....	43
Figure 2.2: (a) Experimental set-up comprised of 6:1 scaled-down model of BOF vessel, and (b) schematic of bottom tuyeres arrangements. ....	45
Figure 2.3: Image processing methodology used in the present work, (a) raw image, (b) monochromatic image, (c) inverted monochromatic image used to calculate exposed area...	46
Figure 2.4: Schematic of solution domain, (b) interior view of computational mesh. ....	51
Figure 2.5: (a) simulated instantaneous gas volume fraction distribution over mid plane, (b) position of all bubble plumes, and time-averaged gas volume fraction distribution at different $\theta$ planes for vessel height of (c) 0.104 m, and (d) 0.204 m, $m_G = 1.3 \times 10^{-3} \text{ kg/s}$ . ....	52
Figure 2.6: Effect of grid resolution on the time- and $\theta$ -averaged air volume fraction distribution at a vessel height of (a) 0.0638 m, and (b) 0.204 m, $m_G = 1.3 \times 10^{-3} \text{ kg/s}$ . ....	53
Figure 2.7: Effect of grid resolution on time-averaged water-phase (a) vertical velocity and (b) turbulent kinetic energy distribution at a vessel height of 0.204 m $m_G = 1.3 \times 10^{-3} \text{ kg/s}$ . ..	54
Figure 2.8: Effect of intercoupling forces on the simulated alpha distribution over XY plane (a) case I (b) case II, (c) case III, (d) case IV, and (e) case V for $m_G = 1.3 \times 10^{-3} \text{ kg/s}$ . ....	56
Figure 2.9: Comparison of measured [40] and predicted $\langle \bar{\alpha}_{G,\theta} \rangle$ profiles at vessel heights (Y) of (a) 0.0603 m, (b) 0.105 m, and (c) 0.204 m $m_G = 1.3 \times 10^{-3} \text{ kg/s}$ . ....	57

Figure 2.10: Comparison of (a) measured [40] and simulated local gas volume fraction fluctuations using (b) $F_D$ , (c) $F_D + F_L$ and (d) $F_D + F_L + F_{TD}$ at point P1( $r = 0.22$ m, $z = 0.2$ m, $\theta = 0^\circ$ ) (location shown in <b>Figure 2.5(a)</b> ), $m_G = 1.3 \times 10^{-3}$ kg/s. ....	59
Figure 2.11: Effect of $m_G$ on on the measured [40] and simulated $\langle \bar{\alpha}_{G,\theta} \rangle$ at vessel heights (Y) of (a) 0.603 m, (b) 0.104 m, and (c) 0.204 m.....	60
Figure 2.12: Comparison of measured [40] and simulated $\alpha_G$ fluctuations at point P1( $r = 0.22$ m, $z = 0.2$ m, $\theta = 0^\circ$ ) (location shown in <b>Figure 2.5(a)</b> ) at $m_G$ of $7.44 \times 10^{-3}$ kg/s.....	62
Figure 2.13: Simulated distribution of (a) instantaneous $\alpha_o$ (b) numerical cells marked with suitable color to identify primary phase in the respective regimes (blue: oil, yellow: water and red: air), instantaneous distribution of $F_D$ for different flow regimes (c) water-dispersed-in-oil ( $F_{DW-o}$ ), (d) oil-dispersed-in-water ( $F_{Do-w}$ ), and air-dispersed-in-oil ( $F_{DG-o}$ ), for $h_o$ of 50 mm, ( $m_G = 1.3 \times 10^{-3}$ kg/s).....	65
Figure 2.14: Schematic of different forces acting on liquid-liquid interface, (red: inertial force $F_I$ exerted by water-phase, black: gravitational force $F_G$ exerted by the oil layer, white: viscous force $F_V$ exerted by the oil layer, and yellow: interfacial tension force $F_\sigma$ acting on oil-water interface). ....	67
Figure 2.15: Simulated instantaneous distribution of (i) $\alpha_o$ and (ii) $\alpha_w$ (superimposed with liquid velocity vector) at different time instants of (a) 4 s, (b) 9 s, and (c) >35 s, over vertical plane $m_G = 1.3 \times 10^{-3}$ kg/s. ....	68
Figure 2.16: Simulated water-phase (a) time-averaged vertical velocity distribution near the oil-water interface ( $Z = 0.27$ m) and (b) velocity vector over mid plane (coloured with vertical velocity) ( $h_o = 15$ mm and $m_G = 1.3 \times 10^{-3}$ kg/s).....	69
Figure 2.17: Simulated distribution of (a) time-averaged $\alpha_G$ and (b) instantaneous $\alpha_w$ superimposed with oil phase (note: black coloured region represent the distribution of oil layer) over vertical plane at $h_o$ of (i) without oil layer, (b) 15 mm, (c) 50 mm, and (d) 100 mm $m_G = 1.3 \times 10^{-3}$ kg/s.....	70
Figure 2.18: Comparison of (i) measured and (ii) simulated oil phase distribution for for $h_o$ of (a) 15 mm, (b) 50 mm and (c) 100 mm, ( $m_G = 1.3 \times 10^{-3}$ kg/s).....	72

Figure 2.19: Reproducibility of measured oil layer distribution for $m_G$ of (i) $3.73 \times 10^{-4} \text{ kg/s}$ , (ii) $7.44 \times 10^{-4} \text{ kg/s}$ , and (iii) $1.3 \times 10^{-3} \text{ kg/s}$ ( $h_o = 15 \text{ mm}$ ) (Brown colour region represents the oil layer).....	73
Figure 2.20: Comparison of measured and simulated oil layer distribution for $h_o$ of (i) 15 mm and (ii) 50 mm, at $m_G$ of (a) $3.73 \times 10^{-4} \text{ kg/s}$ , (b) $7.44 \times 10^{-4} \text{ kg/s}$ , and (c) $1.3 \times 10^{-3} \text{ kg/s}$ .....	75
Figure 2.21: Distribution of oil layer (i) measurements and (ii) simulation at different time instants showing time-evolution of ‘open-eye’ formation corresponding to meandering motion of bubble plumes ( $h_o = 50 \text{ mm}$ and $m_G = 3.74 \times 10^{-4} \text{ kg/s}$ ).....	76
Figure 2.22: Simulated oil volume fraction distribution at $m_G$ of (a) $3.73 \times 10^{-4} \text{ kg/s}$ , (b) $7.44 \times 10^{-4} \text{ kg/s}$ , and (c) $1.3 \times 10^{-3} \text{ kg/s}$ , for $h_o$ of 100 mm. ....	76
Figure 2.23: Comparison of measured and predicted averaged open eye area at different $h_o$ and $m_G$ . ....	77
Figure 3.1: (a) Time evolution of simulated $C_A$ at 8 different locations (P1 to P8) (b) fraction of vessel volume within $\pm 10\%$ of final concentration $m_G = 1.3 \times 10^{-3} \text{ kg/s}$ . ....	88
Figure 3.2: Effect of grid resolution on mixing time (definition II) $m_G = 1.3 \times 10^{-3} \text{ kg/s}$ . 89	
Figure 3.3: Comparison of (i) instantaneous air volume fraction distribution, (ii) water velocity magnitude, (iii) vertical water velocity distribution over vertical planes ( $y = 0.204 \text{ m}$ ), for different $h_o$ of (a) without oil layer, (b) 15 mm, (c) 50 mm, and (d) 100 mm, ( $m_G = 1.3 \times 10^{-3} \text{ kg/s}$ ). ....	
Figure 3.4: Comparison of simulated (a) $\langle \bar{V}_{W,Y} \rangle$ distribution at vessel height of $Y = 0.204 \text{ m}$ , (b) histogram distribution of $\langle \bar{V}_W \rangle$ in the vessel volume with $\alpha_W \geq 0.9$ (see inset of Figure) for different $h_o$ ( $m_G = 1.3 \times 10^{-3} \text{ kg/s}$ ).....	90
Figure 3.5: Comparison of simulated instantaneous distribution of water phase (i) TKE super imposed with oil layer distribution (black region), and (ii) TKE dissipation rate for different $h_o$ of (a) without oil layer, (b) 15 mm, (c) 50 mm, (c) 100 mm, $m_G = 1.3 \times 10^{-3} \text{ kg/s}$ . ....	91

Figure 3.6: Comparison of simulated time-average TKE histogram distribution in the vessel volume with  $\alpha_W \geq 0.9$  (see inset of figure), for different  $h_O$ ,  $m_G = 1.3 \times 10^{-3} \text{ kg/s}$ .....92

Figure 3.7: Comparison of (i)  $\alpha_W$  distribution superimposed with oil layer distribution (black region), instantaneous distribution of (b)  $\bar{V}_W$ , and (c)  $\bar{V}_{W,Y}$  at different  $\rho_O$  of (i)  $919 \text{ kg/m}^3$ , (ii)  $700 \text{ kg/m}^3$ , and (iii)  $500 \text{ kg/m}^3$ , for  $h_O$  of 50 mm, ( $m_G = 1.3 \times 10^{-3} \text{ kg/s}$  and  $\mu_O = 0.055 \text{ Pa.s}$ ).....94

Figure 3.8: Comparison of time-averaged (a) water velocity magnitude, and (b) TKE histogram distribution in the vessel volume with  $\alpha_w \geq 0.9$  for different  $\rho_O$ , ( $m_G = 1.3 \times 10^{-3} \text{ kg/s}$ , and  $\mu_O = 0.055 \text{ Pa.s}$ ).....95

Figure 3.9: Comparison of (i)  $\alpha_G$  distribution superimposed with oil layer distribution (black region), instantaneous distribution of (ii)  $\bar{V}_W$ , and (iii)  $\bar{V}_{W,Y}$  at different  $\mu_O$  of (a)  $0.055 \text{ Pa-s}$ , (b)  $0.005 \text{ Pa-s}$ , and (c)  $0.1 \text{ Pa-s}$ , for  $h_O$  of 50 mm, ( $m_G = 1.3 \times 10^{-3} \text{ kg/s}$  and  $\rho_O = 919 \text{ kg/m}^3$ ).....96

Figure 3.10: Comparison of instantaneous distribution of (a) TKE (b) TKE dissipation rate at different  $\rho_O$  of (i)  $919 \text{ kg/m}^3$ , (ii)  $700 \text{ kg/m}^3$ , and (iii)  $500 \text{ kg/m}^3$ , for  $h_O$  of 50 mm, ( $m_G = 1.3 \times 10^{-3} \text{ kg/s}$  and  $\mu_O = 0.055 \text{ Pa.s}$ ).....98

Figure 3.11: Simulated instantaneous distribution of  $C_A$  over r- $\theta$  plane at vessel height of  $Y = 0.104 \text{ m}$  for different  $m_G$  of (i)  $3.73 \times 10^{-4}$ , (b)  $7.44 \times 10^{-4}$  and (iii)  $1.3 \times 10^{-3} \text{ kg/s}$  at different time instants of (a) 5 s, (b) 10 s, (c) 20 s, and (d) 40 s, (without oil layer). .....99

Figure 3.12: Comparison of simulated and measured [40] mixing time for different  $m_G$ . ... 100

Figure 3.13: Simulated instantaneous distribution of  $C_A$  over r- $\theta$  plane at vessel height of  $Y = 0.104$  for different  $h_O$  of (i) without oil layer, (ii) 15 mm, (iii) 50 mm, and (iv) 100 mm at time instants of (a) 5 s, (b) 10 s, (c) 30 s, (d) 40 s,  $m_G = 1.3 \times 10^{-3} \text{ kg/s}$ . ..... 102

Figure 3.14: Time-evolution of simulated  $C_A$  at 8 locations for  $h_O$  of (a) without oil layer, (b) 15 mm, (c) 50 mm and (d) 100 mm, II for different  $h_O$ ,  $m_G = 1.3 \times 10^{-3} \text{ kg/s}$ ..... 103

Figure 3.16: Comparison of (i) streamlines at different vertical planes ( $Z = 0, 0.1$  and  $0.2 \text{ m}$ ), (ii) 3D surface plot of instantaneous vertical water velocity at vessel height of  $0.204 \text{ m}$ , and

(iii) streamlines over r- $\theta$  plane (vessel height of 0.204 m) for different  $h_o$  of (i) without oil layer, (ii) 15 mm, (iii) 50 mm, and (iv) 100 mm,  $m_G = 1.3 \times 10^{-3} \text{ kg/s}$ . ..... 107

Figure 3.17: Instantaneous distribution of  $D_{AB_{eff}}$  over r- $\theta$  plane at vessel height of 0.204 m for different  $h_o$  of (a) without oil layer, (b) 15 mm, (c) 50 mm, and (d) 100 mm; comparison of simulated histogram of  $D_{AB_{eff}}$  for different  $h_o$ ,  $m_G = 1.3 \times 10^{-3} \text{ kg/s}$ ..... 108

Figure 3.18: Comparison of simulated instantaneous  $C_A$  distribution over r- $\theta$  plane (vessel height of 0.104 m) at different  $\rho_o$  of (i) 919 kg/m<sup>3</sup>, (ii) 700 kg/m<sup>3</sup>, (iii) 500 kg/m<sup>3</sup>, at time instants of (a) 5 s, (b) 10 s, (c) 15 s, and (d) 20 s, for  $h_o$  of 50 mm, ( $m_G = 1.3 \times 10^{-3} \text{ kg/s}$  and  $\mu_o = 0.055 \text{ Pa.s}$ ). ..... 110

Figure 3.19: Comparison of simulated instantaneous  $C_A$  distribution over r- $\theta$  plane (vessel height of 0.104 m) for different  $\mu_o$  of (i) 0.005 Pa-s, (ii) 0.055 Pa-s, (iii) 0.1 Pa-s, at time instant of (a) 5 s, (b) 10 s, (c) 15 s, (d) 20 s,  $h_o$  of 50 mm ( $m_G = 1.3 \times 10^{-3} \text{ kg/s}$  and  $\rho_o = 919 \text{ kg/m}^3$ ). ..... 111

Figure 4.1: Details of (a) top blowing lance, (b) position of tuyeres (blue colour) and top blowing nozzles (red colour), (c) computational domain and (b) numerical grid view..... 119

Figure 4.2: (a) Distribution of computational cells over mid plane with suitable colour to represent different regimes considered for implementation of drag force, (blue: air-dispersed-in-water, green: water-dispersed-in-air, and red: blending region); simulated instantaneous distribution of (b)  $K_{WG_W}$ , (c)  $K_{WG_G}$ , and (d)  $K_{WG_{blend}}$ . ..... 123

Figure 4.3: Effect of grid size on the top air jet velocity distribution for (a) coarse, (b) medium, and (c) fine; comparison of centreline (d) air-jet velocity magnitude and (e) air-jet TKE along vessel height for different grid size at  $m_{G,T}$  of 0.12 kg/s and  $H_l$  of 0.3 m. .... 126

Figure 4.4: Comparison of jet axial velocity for compressible and incompressible flow, at  $m_{G,T}$  of 0.12 kg/s and  $H_l$  of 0.3 m. .... 126

Figure 4.5: Comparison of simulated and calculated cavity depth for (a) different  $m_{G,T}$  at  $H_l$  of 0.3 m, and (b) different  $H_l$  at  $m_{G,T}$  of 0.12 kg/s..... 128

Figure 4.6: Simulated instantaneous (a) top air velocity magnitude, (b) water-phase volume fraction and (c) time-averaged air-phase volume fraction distribution over mid plane ( $m_{G,T}=0.12$ kg/s and $H_l=0.3$ m) .....	129
Figure 4.7: Comparison of simulated (a) $\bar{V}_W$ distribution superimposed with streamlines over vertical plane at mid vessel and (b) $\bar{V}_{W,Y}$ distribution over r- $\theta$ plane at a vessel height of 0.15 m for $m_{G,T}$ of (a) 0 kg/s (bottom blowing), (b) 0.06 kg/s, (c) 0.09 kg/s, and (d) 0.12 kg/s, ( $H_l = 0.3$ m).....	131
Figure 4.8: Comparison of simulated $\langle \bar{V}_{W,Y} \rangle$ distribution at vessel height of 0.15 m over different $\theta$ planes of (a) $0^\circ - 180^\circ$ and (b) $45^\circ - 235^\circ$ , (c) comparison of histogram distribution of $\langle \bar{V}_W \rangle$ in vessel volume with $\alpha_W > 0.9$ for different $m_{G,T}$ , ( $H_l = 0.3$ m). .....	132
Figure 4.9: Simulated instantaneous $\bar{V}_W$ distribution over mid plane ( $\theta = 45^\circ - 235^\circ$ ) for different $m_{G,T}$ of (a) 0 kg/s (bottom blowing), (b) 0.06 kg/s, and (c) 0.12 kg/s, ( $H_l = 0.3$ m).....	134
Figure 4.10: Simulated instantaneous distribution of (a) water volume fraction, (b) water velocity magnitude superimposed with streamlines, and (c) vertical liquid velocity over r- $\theta$ plane under only top blowing conditions, $m_{G,T} = 0.12$ kg/s, $m_{G,B} = 0$ kg/s, $H_l = 0.3$ m)....	135
Figure 4.11: Comparison of simulated (a) $\langle \bar{V}_{W,Y} \rangle$ at a vessel height of 0.15 m over vertical plane at $\theta = 0^\circ-180^\circ$ , and (b) histogram distribution of $\langle \bar{V}_W \rangle$ in the vessel volume with $\alpha_W > 0.9$ , ( $H_l = 0.3$ m). .....	135
Figure 4.12: Comparison of simulated distribution of (i) TKE and (b) TKE dissipation rate over mid plane for $m_{G,T}$ of (a) 0 (bottom blowing), (b) 0.06 kg/s, (c) 0.09 kg/s, and (d) 0.12 kg/s, ( $H_l = 0.3$ m). .....	136
Figure 4.13: Comparison of simulated (a) TKE and (b) TKE dissipation rate histogram distribution (over an iso-volume of $\alpha_W \geq 0.9$ ) for different $m_{G,T}$ at $H_l = 0.3$ m.....	137
Figure 4.14: Comparison of simulated air jet velocity distribution for $H_l$ of (a) 0.45 m and (b) 0.6 m, and (c) comparison of radial position of max jet velocity variation with distance from nozzle exit for different $H_l$ .....	138

Figure 4.15: Comparison of cavity shape/ mode (iso-surface of $\alpha_W = 0.5$ ) for $m_{G,T}$ (a) 0.06 kg/s, (b) 0.12 kg/s, of 0.3 m; and (c) $H_l$ of 0.3 m at $m_{G,T}$ of 0.12 kg/s.....	138
Figure 4.16: Comparison of simulated distribution $\bar{V}_W$ superimposed with streamlines for $H_l$ of (a) 0.45 m, and (b) 0.6 m, and (c) water-phase time-averaged vertical liquid velocity distribution at $Y = 0.15$ m, (d) histogram distribution of $\langle \bar{V}_W \rangle$ for different $H_l$ .....	140
Figure 4.17: Simulated instantaneous distribution of $C_A$ over r- $\theta$ plane at a vessel height of 0.104 m for different $m_{G,T}$ of (i) 0 kg/s (bottom blowing), (ii) 0.06 kg/s, (iii) 0.09 kg/s, (iv) 0.12 kg/s and (v) 0.12 kg/s (only top blowing) at different time instants of (a) 2 s, (b) 5s, (c) 20 s, and (d) 30 s, ( $H_l = 0.3$ m).....	143
Figure 4.18: Time-evaluation of simulated $C_A$ at different locations (P1 to P8) for $m_{G,T}$ of (a) 0 kg/s (bottom blowing), (b) 0.6 kg/s, (c) 0.12 kg/s, at $H_l$ of 0.3 m; and (d) $H_l$ of 0.6 m at $m_{G,T}$ of 0.12 kg/s.....	144
Figure 4.19: Comparison of simulated distribution of $\bar{V}_{W,\theta}$ over a circular plane at PCD of 0.7 for $m_{G,T}$ of (a) 0 kg/s, (b) 0.06 kg/s, and (c) 0.12 kg/s; (d) variation of $\bar{V}_{W,\theta}$ along $\theta$ at a vessel height of 0.15 m, ( $H_l$ of 0.3 m). .....	147
Figure 4.20: Simulated 3D streamlines injected from top central axis at 10 s (coloured with tracer mass fraction) for different $m_{G,T}$ of (a) 0 kg/s (bottom blowing), (b) 0.06 kg/s, and (c) 0.12 kg/s, ( $H_l$ of 0.3 m).....	148
Figure 4.21: Comparison of simulated distribution of $C_A$ over r- $\theta$ plane at vessel height of 0.104 m for $H_l$ of (i) 0.45 m and (ii) 0.6 m at different time instants of (a) 2 s, (b) 5 s (c) 30 s, and (d) 40 s, ( $m_{G,T} = 0.12$ kg/s). .....	149
Figure 4.22: Comparison of Simulated 3D streamlines injected from top central axis at 10 s (coloured with tracer mass fraction) for $H_l$ of (a) 0.45 m and (b) 0.6 m, ( $m_{G,T} = 0.12$ kg/s). .....	150
Figure 5.1: (i) Experimental setup, (ii) image processing methodology: (a) raw image, (b) monochromatic image, (c) outlines of oil layer extracted using multiple images, and (d) averaged distribution of oil layer obtained using MATLAB. ....	159

Figure 5.2: (a) Solution domain (all dimensions are in mm), (b) computational mesh over a vertical plane, and (c) grid refinement near the inlet. ....	164
Figure 5.3: Comparison of measured, and simulated oil layer distribution for $m_G$ of (a) $2.33 \times 10^{-5} \text{ kg/s}$ , (b) $4.66 \times 10^{-5} \text{ kg/s}$ , $h_o = 15\text{mm}$ . ....	166
Figure 5.4: Comparison of measured, and simulated octane layer distribution for $m_G$ of (a) $2.33 \times 10^{-5} \text{ kg/s}$ , (b) $4.66 \times 10^{-5} \text{ kg/s}$ , $h_o = 15\text{mm}$ . ....	167
Figure 5.5: Effect of grid resolution on the (a) liquid-liquid interface shape at (b) time-averaged liquid velocity (c) vorticity at $Y = 0.28 \text{ m}$ , $Z = 0.1 \text{ m}$ ( $h_o = 15 \text{ mm}$ , $\rho_o = 919 \text{ kg/m}^3$ , $\mu_o = 0.055 \text{ Pa}\cdot\text{s}$ , $\sigma_{o-g} = 0.04 \text{ N/m}$ , $\sigma_{o-w} = 0.056 \text{ N/m}$ , $d_B = 5 \text{ mm}$ , $m_G = 4.66 \times 10^{-5} \text{ kg/s}$ ). ....	168
Figure 5.6: Schematic of (a) undeformed and (b) deformed liquid-liquid interface, (c) schematic showing different forces acting on the deformed interface (blue: inertial force $F_I$ exerted by water, black: gravitational force $F_G$ exerted by the oil phase, yellow: viscous force $F_V$ exerted by oil phase, and white: interfacial tension force $F_\sigma$ acting on the oil-water interface). ....	169
Figure 5.7: Simulated (i) instantaneous $\alpha_o$ distribution and (ii) iso-surface of oil (at $\alpha_o = 0.5$ ) superimposed with bubble positions (colored by bubble vertical velocity) at different time instants of (a) 0.5 s, (b) 3 s, (c) 5 s, ( $h_o = 15 \text{ mm}$ , $m_G = 4.66 \times 10^{-5} \text{ kg/s}$ ). ....	171
Figure 5.8: Simulated instantaneous (i) $\alpha_o$ distribution superimposed with liquid velocity vector and (ii) iso-surface of oil (at $\alpha_o = 0.9$ ) superimposed with bubble positions (colored by bubble vertical velocity) for $h_o$ of (a) 15 mm, (b) 50 mm, and (c) 100 mm ( $\rho_o = 919 \text{ kg/m}^3$ , $\mu_o = 0.055 \text{ Pa}\cdot\text{s}$ , $\sigma_{o-g} = 0.04 \text{ N/m}$ , $\sigma_{o-w} = 0.056 \text{ N/m}$ , $d_B = 5 \text{ mm}$ , $m_G = 4.66 \times 10^{-5} \text{ kg/s}$ ). ....	172
Figure 5.9: Effect of (a) $h_o$ and (b) $\rho_o$ on the time-averaged vertical liquid velocity distribution near the oil-water interface ( $Y = 0.27 \text{ m}$ ), ( $\sigma_{o-g} = 0.04 \text{ N/m}$ , $\sigma_{o-w} = 0.056 \text{ N/m}$ , $d_B = 5 \text{ mm}$ , $m_G = 4.66 \times 10^{-5} \text{ kg/s}$ ). ....	173
Figure 5.10: Effect of $\rho_o$ on the simulated instantaneous (i) $\alpha_o$ distribution superimposed with liquid velocity vectors and (ii) iso-surface of $\alpha_o$ (a) superimposed with bubble positions	

(colored with bubble vertical velocity) for  $\rho_o$  of (a)  $493 \text{ kg/m}^3$ , (b)  $800 \text{ kg/m}^3$ , and (c)  $919 \text{ kg/m}^3$ , ( $h_o = 50 \text{ mm}$ ,  $\mu_o = 0.055 \text{ Pa.s}$ ,  $\sigma_{o-g} = 0.04 \text{ N/m}$ ,  $\sigma_{o-w} = 0.056 \text{ N/m}$ ,  $d_B = 5 \text{ mm}$ ,  $m_G = 4.66 \times 10^{-5} \text{ kg/s}$ ). ..... 175

Figure 5.11: Simulated instantaneous iso-surface of oil layer ( $\alpha_o = 0.5$ ) superimposed with the velocity vector for  $m_G$  of (a)  $4.66 \times 10^{-5} \text{ kg/s}$ , (b)  $2.33 \times 10^{-4} \text{ kg/s}$ , (c) time-averaged vertical liquid velocity distribution for  $\rho_o$  of  $493 \text{ kg/m}^3$  ( $h_o = 50 \text{ mm}$ ,  $\mu_o = 0.055 \text{ Pa.s}$ ,  $\sigma_{o-g} = 0.04 \text{ N/m}$ ,  $\sigma_{o-w} = 0.056 \text{ N/m}$ ,  $d_B = 5 \text{ mm}$ ). ..... 176

Figure 5.12: Effect of  $\mu_o$  on the simulated instantaneous (i)  $\alpha_o$  distribution superimposed with liquid velocity vectors and (ii) iso-surface of oil layer (at  $\alpha_o = 0.9$ ) superimposed with bubble position (coloured with bubble vertical velocity) for  $\mu_o$  of (a)  $0.005 \text{ Pa.s}$ , (b)  $0.055 \text{ Pa.s}$ , and (c)  $0.1 \text{ Pa.s}$  ( $h_o = 50 \text{ mm}$ ,  $\rho_o = 919 \text{ kg/m}^3$ ,  $\sigma_{o-g} = 0.04 \text{ N/m}$ ,  $\sigma_{o-w} = 0.056 \text{ N/m}$ ,  $m_G = 4.6 \times 10^{-5} \text{ kg/s}$ ,  $d_B = 5 \text{ mm}$ ). ..... 177

Figure 5.13: Effect of (a)  $\mu_o$  on the viscous stress and (b)  $\sigma_{o-w}$  on the interfacial tension force acting on the oil-water interface (iso-surface of  $\alpha_w = 0.5$ ) ( $h_o = 50 \text{ mm}$ ,  $\rho_o = 493 \text{ kg/m}^3$ ,  $\sigma_{o-g} = 0.04 \text{ N/m}$ ,  $\sigma_{o-w} = 0.056 \text{ N/m}$ ,  $m_G = 4.6 \times 10^{-5} \text{ kg/s}$ ,  $d_B = 5 \text{ mm}$ ). ..... 178

Figure 5.14: Effect of  $\mu_o$  on the simulated time-averaged (a) bubble rise velocity and (b) bubble volume fraction distribution at a column height of  $Y = 0.31 \text{ m}$  ( $h_o = 50 \text{ mm}$ ,  $\rho_o = 919 \text{ kg/m}^3$ ,  $\sigma_{o-g} = 0.04 \text{ N/m}$ ,  $\sigma_{o-w} = 0.056 \text{ N/m}$ ,  $m_G = 4.6 \times 10^{-5} \text{ kg/s}$ ,  $d_B = 5 \text{ mm}$ ). ..... 179

Figure 5.15: Effect of  $\sigma_{o-w}$  on the simulated instantaneous (i) oil volume fraction distribution superimposed with liquid velocity vectors and (ii) iso-surface of oil (at  $\alpha_o = 0.9$ ) superimposed with bubble position (coloured with bubble vertical velocity) for  $\sigma_{o-w}$  of (a)  $0.028 \text{ N/m}$ , (b)  $0.056 \text{ N/m}$ , and (c)  $0.112 \text{ N/m}$ , ( $h_o = 50 \text{ mm}$ ,  $\mu_o = 0.055 \text{ Pa.s}$ ,  $\sigma_{o-g} = 0.04 \text{ N/m}$ ,  $d_B = 5 \text{ mm}$ ,  $m_G = 4.66 \times 10^{-5} \text{ kg/s}$ ). ..... 180

Figure 5.16: Effect of  $\sigma_{o-w}$  on the simulated instantaneous oil layer distribution for  $\sigma_{o-w}$  of (a)  $0.056 \text{ N/m}$ , and (b)  $0.56 \text{ N/m}$ , ( $h_o = 50 \text{ mm}$ ,  $\rho_o = 919 \text{ kg/m}^3$ ,  $\mu_o = 0.055 \text{ Pa.s}$ ,  $\sigma_{o-g} = 0.04 \text{ N/m}$ ,  $d_B = 5 \text{ mm}$ ,  $m_G = 4.66 \times 10^{-5} \text{ kg/s}$ ). ..... 181

Figure 5.17: Effect of  $m_G$  on simulated instantaneous (i)  $\alpha_o$  distribution superimposed with liquid velocity vector and (ii) iso-surface of oil (at  $\alpha_o = 0.9$ ) superimposed with bubble

positions (colored with bubble vertical velocity) for  $m_G$  of (a)  $4.6 \times 10^{-6} \text{ kg/s}$ , (b)  $2.33 \times 10^{-5} \text{ kg/s}$ , (c)  $4.6 \times 10^{-5} \text{ kg/s}$ , (d)  $2.33 \times 10^{-4} \text{ kg/s}$ , and (e)  $4.6 \times 10^{-4} \text{ kg/s}$ , ( $h_O = 50 \text{ mm}$ ,  $\rho_O = 919 \text{ kg/m}^3$ ,  $\mu_O = 0.055 \text{ Pa.s}$ ,  $\sigma_{O-G} = 0.04 \text{ N/m}$ ,  $\sigma_{O-W} = 0.056 \text{ N/m}$ ,  $d_B = 5 \text{ mm}$ ). ..... 182

Figure 5.18: Effect of  $m_G$  on the simulated time-averaged vertical water velocity distribution ( $h_O = 50 \text{ mm}$ ,  $\rho_O = 919 \text{ kg/m}^3$ ,  $\mu_O = 0.055 \text{ Pa.s}$ ,  $\sigma_{O-G} = 0.04 \text{ N/m}$ ,  $\sigma_{O-W} = 0.056 \text{ N/m}$ ,  $d_B = 5 \text{ mm}$ ). ..... 183

Figure 5.19: Effect of  $d_B$  on the simulated instantaneous (i) oil volume fraction distribution superimposed with liquid velocity vector (ii) iso-surface of oil (at  $\alpha_O = 0.9$ ) superimposed with bubble positions (colored with bubble vertical velocity) for  $d_B$  of (a) 5 mm, (b) 2 mm, and (c) 0.5 mm, ( $h_O = 50 \text{ mm}$ ,  $\rho_O = 919 \text{ kg/m}^3$ ,  $\mu_O = 0.055 \text{ Pa.s}$ ,  $\sigma_{O-G} = 0.04 \text{ N/m}$ ,  $\sigma_{O-W} = 0.056 \text{ N/m}$ ). ..... 184

Figure 5.20: Effect of  $d_B$  on the simulated time-averaged (a) bubble vertical velocity and (b) bubble volume fraction distribution at column height of  $Y = 0.31 \text{ m}$  ( $h_O = 50 \text{ mm}$ ,  $\rho_O = 919 \text{ kg/m}^3$ ,  $\mu_O = 0.055 \text{ Pa.s}$ ,  $\sigma_{O-G} = 0.04 \text{ N/m}$ ,  $\sigma_{O-W} = 0.056 \text{ N/m}$ ,  $m_G = 4.66 \times 10^{-5} \text{ kg/s}$ ). ..... 185

Figure 5.21: Effect of  $\mu_W$  on the simulated instantaneous oil layer distribution for  $\mu_W$  of (a)  $0.001 \text{ Pa.s}$  (b)  $0.01 \text{ Pa.s}$ , ( $h_O = 50 \text{ mm}$ ,  $\rho_O = 919 \text{ kg/m}^3$ ,  $\mu_O = 0.055 \text{ Pa.s}$ ,  $\sigma_{O-G} = 0.04 \text{ N/m}$ ,  $\sigma_{O-W} = 0.056 \text{ N/m}$ ,  $d_B = 5 \text{ mm}$ ,  $m_G = 4.66 \times 10^{-5} \text{ kg/s}$ ). ..... 186

Figure 5.22: Regime map displaying the oil-water interface topologies as a function of  $Fr^*$  and  $Ca$  (Darker the shades higher the dominance of respective force. The lines shown as boundaries of the individual regime are provided only as a visual aid and do not actually demarcate the boundaries. Moreover, the grey colour solid, dashed, dashed-dot and dotted lines represent the effect of respectively at different conditions). ..... 188

## List of Table

Table 2.1: Physical properties of the working fluids .....	46
Table 2.2: Different interphase momentum exchange models used in the present work.....	55
Table 2.3: Effect of $h_o$ and $m_G$ on the dimensionless numbers.....	71
Table 3.1: Physical properties of working fluids considered in the present work.....	85
Table 3.2: Effect of $h_o$ , $\rho_o$ and $\mu_o$ on dimensionless numbers .....	92
Table 3.3: Effect of $h_o$ on volume-averaged TKE dissipation rate .....	91
Table 3.4: Comparison of simulated mixing time with the measurements [40] for different $m_G$ (without oil layer) .....	100
Table 3.5: Comparison of mixing time for different $h_o$ and $m_G$ .....	103
Table 3.6: Effect of $\rho_o$ and $\mu_o$ on simulated mixing time .....	111
Table 4.1: Quantifications of specific kinetic energy input by top blowing, available in liquid- phase and Energy index for different blowing conditions. ....	141
Table 4.2: Comparison of simulated mixing time for bottom, only top and combined blowing .....	145
Table 4.3: Comparison of simulated mixing time for different $H_l$ .....	150
Table 5.1: Operating conditions used in the present work.....	164
Table 5.2: Comparison of measured and predicted exposed area .....	167
Table 5.3: Effect of $h_o$ and $\rho_o$ on dimensionless number and interface topology .....	174
Table 5.4: Effect of $\mu_o$ and $\sigma_{o-w}$ on dimensionless numbers and interface topology.....	181
Table 5.5: Effect of $m_G$ and $d_B$ on the dimensionless number .....	184

## Nomenclature

H	Liquid bath height, m
g	Gravitational acceleration, m/s <sup>2</sup>
Re <sub>b</sub>	Bubble Reynold's number, -
$E\ddot{o}$	Eotvos number, -
Ca	Capillary number
$Fr^*$	Modified Froud number, -
$m_G$	Gas mass flowrate, kg/s
$\vec{M}$	Interphase momentum exchange force, N/ m <sup>3</sup>
P	Pressure, N/m <sup>2</sup>
$\vec{U}$	Mean velocity, m/s
$\vec{F}_D$	Drag force, N/m <sup>3</sup>
C <sub>D</sub>	Drag coefficient, -
$\vec{F}_L$	Lift force, N/m <sup>3</sup>
C <sub>L</sub>	Lift coefficient, -
$\vec{F}_{TD}$	Turbulent dispersion force, N/m <sup>3</sup>
C <sub>TD</sub>	Turbulent dispersion coefficient, -
$K_{cd}$	Momentum exchange coefficient, kg/m <sup>3</sup> s
$h_O$	Oil layer thickness, mm
$C_A$	Tracer mass fraction,-
D	Diffusivity, m <sup>2</sup> /s
X, Y, Z	Spatial coordinates (along the width, height, and depth respectively), m
$h_c$	Depth of cavity, m
$H_l$	Lance height, m
$\bar{V}_W$	Instantaneous water-phase velocity magnitude, m/s
$\bar{V}_{W,Y}$	Instantaneous water-phase vertical velocity, m/s
$\bar{V}_{W,\theta}$	Instantaneous water-phase circumferential velocity, m/s
$\langle \bar{V}_W \rangle$	Time-averaged water phase velocity magnitude, m/s
$\langle \bar{V}_{W,Y} \rangle$	Time-averaged water phase vertical velocity, m/s
$\langle \bar{\alpha}_{G,\theta} \rangle$	Time- and- $\theta$ -averaged gas volume fraction, -

### Greek letters

$\alpha$	Volume fraction, -
$\mu$	Viscosity, Pa-s
$\rho$	Density, kg/m <sup>3</sup>
$k$	Turbulent kinetic energy, m <sup>2</sup> /s <sup>2</sup>
$\varepsilon$	Turbulent kinetic energy dissipation rate, m <sup>2</sup> /s <sup>3</sup>
$\bar{\tau}$	Shear stress, N/m <sup>2</sup>
$\sigma$	Surface tension coefficient, N/m

## Subscripts

A	Actual
M	Model
i	i <sup>th</sup> phase
G	Air/ gas
O	Oil/ slag
W	Water
lam	Laminar
eff	Effective
t	Turbulent
T	Top blowing
B	Bottom blowing
c	Continuous
d	Dispersed

## Acronyms

BOF	Basic Oxygen Furnace
E-E	Euler-Euler
CFD	Computational Fluid Dynamics
VOF	Volume of fluid
DPM	Discrete Particle Method
PBM	Population Balance Method
PCD	Pitch to circle diameter ratio
RANS	Reynolds Averaged Navier-Stoke equation
TKE	Turbulent kinetic energy